

Article

Cogging Torque Reduction of a Flux-Intensifying Permanent Magnet-Assisted Synchronous Reluctance Machine with Surface-Inset Magnet Displacement

Mihály Katona [†] and Tamás Orosz ^{*,†}

Propulsion Technology and Power Electronics, Széchenyi István University, 1. Egyetem tér,
HU-9026 Győr, Hungary; katona.mihaly@sze.hu

* Correspondence: orosz.tamas@sze.hu

† These authors contributed equally to this work.

Abstract

This paper investigates the impact of permanent magnet (PM) displacement and flux barrier extension on cogging torque in flux-intensifying permanent magnet-assisted synchronous reluctance machines (FI-PMa-SynRMs) with surface-inset PMs. Unlike prior work centred on average torque, torque ripple, or inductance, we focus on cogging torque, a key driver of noise and vibration. Four rotor configurations are evaluated via finite element analysis of ~20,000 designs per configuration generated during NSGA-II multi-objective optimisation. To avoid bias from near-duplicate designs, we introduce Euclidean distance-based medoid filtering, which enforces a minimum separation of models within each configuration. The cross-configuration similarity is measured by Euclidean distance over common design variables. Results show that PM displacement alone does not substantially reduce cogging torque, while flux barrier extension alone yields reductions of up to ~25%. Combining PM displacement with flux barrier extension achieves up to a ~30% reduction in cogging torque, often maintaining average torque and lowering torque ripple. This study provides a comparative framework for mitigating cogging torque in FI-PMa-SynRMs and clarifies the trade-offs revealed by similarity-based analyses.



Academic Editor: Sérgio Cruz

Received: 17 September 2025

Revised: 30 September 2025

Accepted: 15 October 2025

Published: 17 October 2025

Citation: Katona, M.; Orosz, T. Cogging Torque Reduction of a Flux-Intensifying Permanent Magnet-Assisted Synchronous Reluctance Machine with Surface-Inset Magnet Displacement. *Energies* **2025**, *18*, 5492. <https://doi.org/10.3390/en18205492>

Copyright: © 2025 by the authors. Licensee MDPI, Basel, Switzerland. This article is an open access article distributed under the terms and conditions of the Creative Commons Attribution (CC BY) license (<https://creativecommons.org/licenses/by/4.0/>).

Keywords: cogging torque; synchronous reluctance; similarity metrics

1. Introduction

Driven by the rapid adoption of electric vehicles, the number of electric motors reaching their end-of-life (EOL) stage is set to rise markedly in the coming years [1]. In parallel, machines are required to satisfy ever-stricter expectations from policymakers and environmentally conscious consumers, in line with circular economy (CE) principles [2]. The European Environment Agency (EEA) emphasises that reuse, remanufacture, and recycling should be designed into products from the outset and that new processes must account for future access to rare earth elements (REEs) [3,4]. The remanufacture of electric machines aims to extend service life and, as a core CE strategy, prioritises non-destructive disassembly, the refurbishment of components, and the reuse of intact parts. Unlike basic refurbishment, remanufacturing targets the same quality standard as a newly manufactured product [5]. The global recycling rate of REE-based materials remains below 3% [6]. A major barrier is the challenging disassembly of interior permanent magnet (PM) machines, where PMs are adhesively bonded into the rotor stack. Novel rotor topologies with inset PMs placed along the circumference offer a route to facilitate disassembly [7]. Technologies that

enable the recovery and reuse of REEs from electrical machines are particularly important for countries without domestic REE deposits [8]. A complementary research direction pursues ferrite PMs, which are more widely available; however, their lower magnetic performance relative to neodymium-based PMs necessitates improved machine topologies.

Permanent magnet-assisted synchronous reluctance machines (PMa-SynRMs) using ferrite PMs can provide a cost-effective and environmentally favourable alternative to other permanent magnet synchronous machines (PMSMs) [4,9], as demonstrated by the SYRNEMO and TELL projects in small electric vehicles [10–12]. A notable variant is the flux-intensifying PMa-SynRM (FI-PMa-SynRM), in which the PMs are inset on the rotor surface along the d -axis rather than embedded in q -axis flux barriers; the reluctance torque remains the dominant component over the magnetic torque. This motor type has been shown to deliver high output torque and low torque ripple while requiring only a limited amount of PM material, thereby reducing the risk of irreversible demagnetisation [7,13,14].

An FI-PMa-SynRM with surface-inset PMs can deliver substantial torque with limited PM volume. The study reported in [13] investigated (i) the displacement of the magnet flux barrier (MFB; Figure 1), (ii) the extension of the MFB, and (iii) PM displacement with MFB extension. The results indicated that extending the MFB, i.e., making the MFB wider than the PM, together with a counter-clockwise PM shift, has little effect on average torque over extension angles ranging from -5° to 5° (1° increments), whereas the torque ripple spans 5% to 30%, implying high sensitivity.

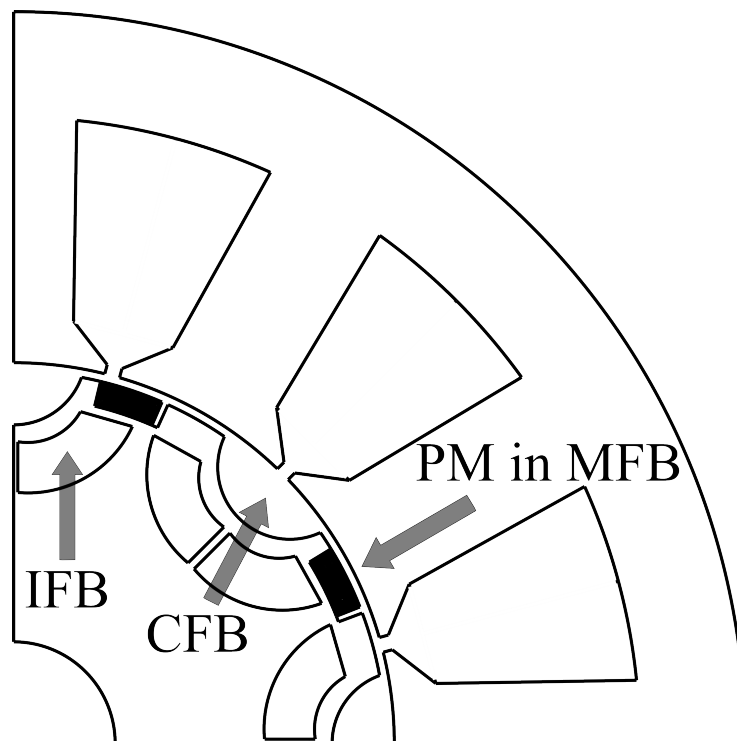


Figure 1. One-fourth of the investigated FI-PMa-SynRM with surface-inset PMs. Abbreviations: PM—permanent magnet; MFB—magnet flux barrier; CFB—cut-off flux barrier; IFB—internal flux barrier.

Nevertheless, cogging-torque variation was not the focus of [13], nor of studies centred on average torque measurement [14], field weakening analysis [15], or inductance calculation [16]. Accordingly, this paper examines how PM displacement and the presence of air barriers adjacent to the PMs—arising from MFB extension—affect the cogging torque in an FI-PMa-SynRM.

Specific combination of PM displacement can reduce cogging torque, even without cut-off (CFBs) and internal (IFBs) flux barriers by exploiting different repeating units in the

absence of an extended MFB [17]. Introducing MFB extension and bidirectional shifting can further reduce torque ripple [18]; however, cogging torque has not been treated separately, despite its role in noise and vibration. Alternative mitigation strategies include rotor skewing [19], slot-opening optimisation [20], and PM-edge slotting/shaping [21–23].

This work investigates four rotor configurations of the same FI-PMa-SynRM: (A) no PM displacement and no MFB extension, (B) no PM displacement with MFB extension, (C) PM displacement without MFB extension, and (D) PM displacement with MFB extension. Comparisons are based on the NSGA-II optimisation histories, comprising ~20,000 finite element analysis (FEA) cases per configuration. Similarity across configurations is defined via the Euclidean distance over the shared design variables, and within a configuration, near-duplicates are removed using a Euclidean distance-based medoid filtering step to avoid biased comparisons.

Section 2 contains descriptions of the models and means of comparison, including data refining, while Section 3 summarises the results and deductions. Section 4 contains the conclusion of this investigation.

2. Methodology

A two-dimensional finite element cross-sectional simulation is performed for a three-phase, star-connected, 0.7 kW FI-PMa-SynRM (Figure 1). The prototype is a downscaled design intended for nominal values of 48 V and 60 A, with particular emphasis on cogging torque. The machine has eight poles and twelve slots with possible unidirectional (counter-clockwise) PM displacement. In such a case, two poles with symmetric boundary conditions are used throughout, corresponding to one-quarter of the 44 mm diameter rotor. The stator is identical across all configurations and is therefore omitted from the figures; it has concentrated windings, an 86.5 mm stator diameter, a 40 mm stack length, and a 1 mm air gap, as shown in Figure 1. Parametric finite element models and torque calculations are automated using py2FEMM [24], a Python 3.10 interface for the Finite Element Method Magnetics solver [25]. To evaluate the average torque and torque ripple, the current condition was set at 30 A/mm², which represents the peak current and is an exceptional condition inherited from a previous study [7]. However, this does not affect the outcome of the present study, as the results are based on relative torque comparisons under the same current condition. Furthermore, the present investigation emphasises cogging torque, which is not affected by the load condition. The geometry of the models is presented later on in this section. The material properties are based on laboratory measurements [26] of the remanufactured machine’s stator steel and the Fe-6.5 wt%Si alloy intended for the 3D-printed rotor. The torque output is evaluated over one period (0° to 15°) with a 1° resolution.

The dataset analysed in this paper comprises the NSGA-II optimisation histories for four rotor configurations (cases A–D) of the above-described machine, each with approximately 20,000 candidate designs, obtained as part of a previous investigation [7]. That study examined the optimisation process and robustness of FI-PMa-SynRM designs employing surface-inset PMs with both bidirectional and unidirectional PM displacement. Variations in rotor dimensions were evaluated for their impact on average torque, torque ripple, and cogging torque using the Taguchi method in relation to an optimal design. The optimal design was obtained via NSGA-II and selected with the SPOTIS and TOPSIS multi-criteria decision-making methods. The selection of an optimal machine is not the aim of the present investigation; for selection, see [7]. To investigate sensitivity, geometric and angular design variables had resolutions of 0.01 mm and 0.01°, respectively. The results indicated that comparable torque can be achieved with less PM volume when PM displacement and air barriers are employed and that the design is less sensitive to assembly-induced PM

displacement than to steel laser-cutting tolerances. However, because air gaps adjacent to the PMs were not isolated as independent variables and the sample size was smaller, those conclusions were primarily robustness-oriented [7]. The present work isolates and compares the effects of unidirectional PM displacement and the presence of air barriers adjacent to the PMs and quantifies their impact on the torque components. The following sections provide detailed descriptions of the considered rotor configurations.

2.1. Models for Comparison

The design variables and their optimisation ranges are summarised in Table 1 for case A, case B, case C, and case D. The Opt. Range (optimisation range) column contains the range that the variables actually take during the NSGA-II optimisation. The Opt. Range of the design variable (X_5 , $X \in [A, B, C, D]$ which is the height of the IFB) is 0.15 mm higher than the Set Range. The Set Range is the preliminarily set optimisation range. This difference is only possible because the geometric feasibility constraints may overwrite the population of a generation. Still, this deviation does not cause any feasibility problems at the torque, geometrical, or manufacturing level.

Table 1. Design variables and their range for the investigated models, where Set Range is the preliminarily set optimisation range and Opt. Range is the range that the variables actually take during the NSGA-II optimisation. PM—permanent magnet; MFB—magnet flux barrier; CFB—cut-off flux barrier; IFB—internal flux barrier.

Variables	Meaning	Set Range	Opt. Range
A_1, B_1, C_1, D_1	Opening angle of CFB	15–25 deg	15–25 deg
A_2, B_2, C_2, D_2	Included angle of CFB	60–140 deg	75.2–140 deg
A_3, B_3, C_3, D_3	Distance between the CFB and IFB	0.5–4 mm	0.5–3.75 mm
A_4, B_4, C_4, D_4	Width of the rib at IFB	0–1 mm	0–1 mm
A_5, B_5, C_5, D_5	Height of IFB	0.5–4 mm	0.5–4.15 mm
A_6, B_6, C_6, D_6	Distance between the PM and IFB	0.5–1 mm	0.51–0.82 mm
A_7, B_7, C_7, D_7	Height of the PM	1.5–2 mm	1.51–1.99 mm
A_8, B_8, C_8, D_8	Width of the PM	10–15 deg	10–15 deg
B_9, D_{10}	Width of MFB	10–18 deg	11.05–18 deg
C_9, D_9	Shifting angle of PM (and MFB)	0–8 deg	0–7.81 deg

2.1.1. Case A Without PM Displacement and Without MFB Extension

FI-PMa-SynRM case A (Figure 2) serves as the baseline for the subsequent rotor configurations. In this case, there is no PM shifting and no MFB extension; consequently, no air barrier is present adjacent to the inset PMs, consistent with [7,13–16]. The design variables are summarised in Table 1. Figure 3 shows the normalised distribution of the design-variable values, where the x -axis is the normalised range (0 denotes the lower bound and 1 is the upper bound) and the y -axis is the frequency of occurrence in the optimisation history. The NSGA-II optimisation tends to push the CFB opening angle (A_1) and the CFB included angle (A_2) towards the upper ends of their ranges, whereas the IFB rib width (A_4), the PM–IFB distance (A_6), and the PM height concentrate near the lower ends of their ranges. In the following cases, the presence of additional design variables may alter these distributions.

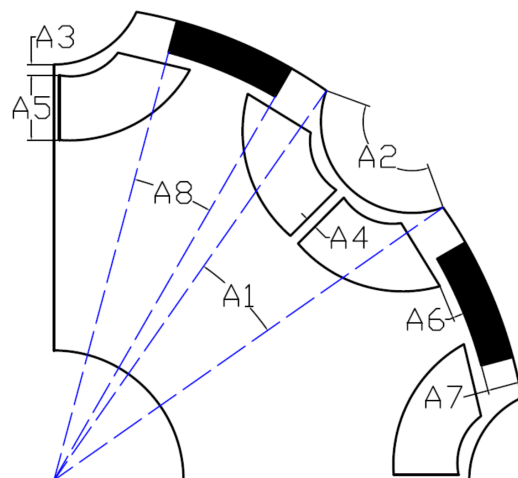


Figure 2. Design variables of case A.

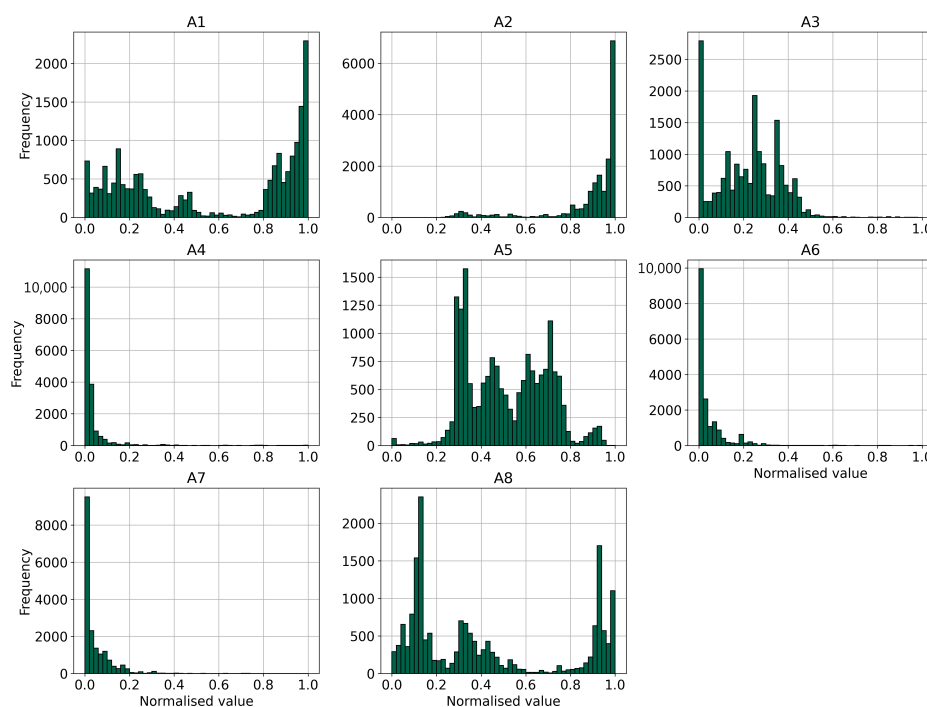


Figure 3. Distribution of the design variables based on the NSGA-II optimisation history of case A.

2.1.2. Case B Without PM Shifting but with MFB Extension

Case B (Figure 4) extends case A by introducing design variable B_9 , i.e., the width of the MFB, which enables an air barrier adjacent to the inset PMs. Increasing B_9 beyond the PM width creates two narrow air barriers flanking each PM along the MFB (not to be confused with the machine air gap). When B_9 is not introduced—as in case A—the MFB width coincides with the PM width, the PM side faces are bounded by steel, and no lateral air barrier exists; all other rotor features remain identical. Figure 5 shows the normalised distribution of the design variables: on the x-axis, 0 denotes the lower bound and 1 is the upper bound of each variable; the y-axis gives the frequency of occurrence in the optimisation history. Relative to case A, there are no material differences in the shared variables (X_1-X_7 ($X \in \{A, B\}$)). The presence of the air barrier primarily affects the PM width (A_8 vs. B_8): in case B, the PM width concentrates near the upper bound of its optimisation range. The implications for torque are discussed in Section 3.

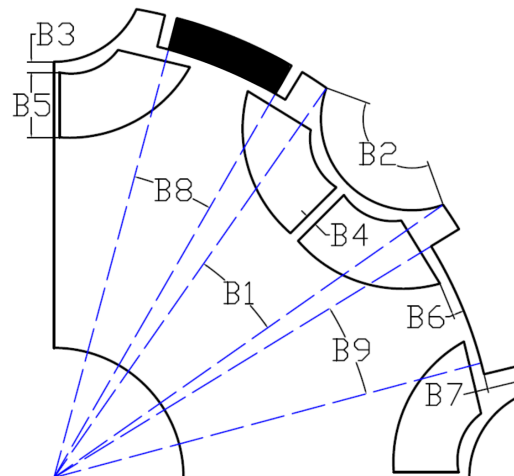


Figure 4. Design variables of case B.

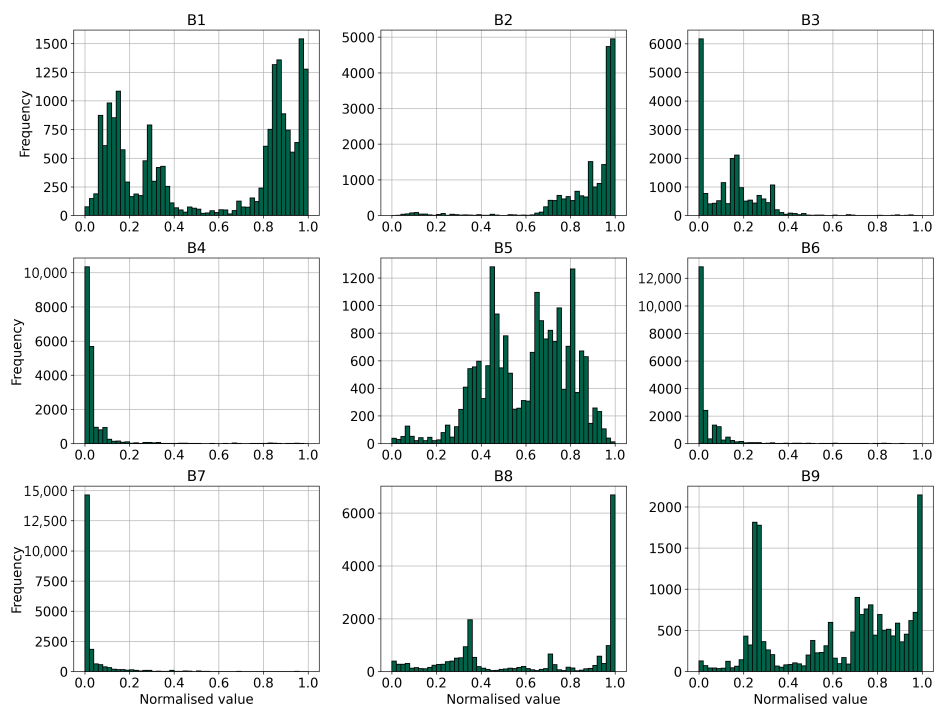


Figure 5. Distribution of the design variables based on the NSGA-II optimisation history of case B.

2.1.3. Case C with PM Shifting but Without MFB Extension

Case C (Figure 6) extends case A by introducing design variable C_9 , which represents the PM shifting angle. As in case A, the MFB width equals the PM width, so no lateral air barrier forms next to the inset PMs. Unlike case A—where the PM is centred—here, the PM is shifted unidirectionally (counter-clockwise) by C_9 with respect to the d -axis, introducing local pole asymmetry; all other rotor features are identical to case A. Figure 7 shows the normalised distribution of the design variables: on the x -axis, 0 denotes the lower bound and 1 is the upper bound; the y -axis indicates the frequency of occurrence in the optimisation history. Relative to Case A, there are no material differences in most variables, except for the CFB opening angle (C_1), which shifts markedly towards the upper bound. The implications for torque are discussed in Section 3.

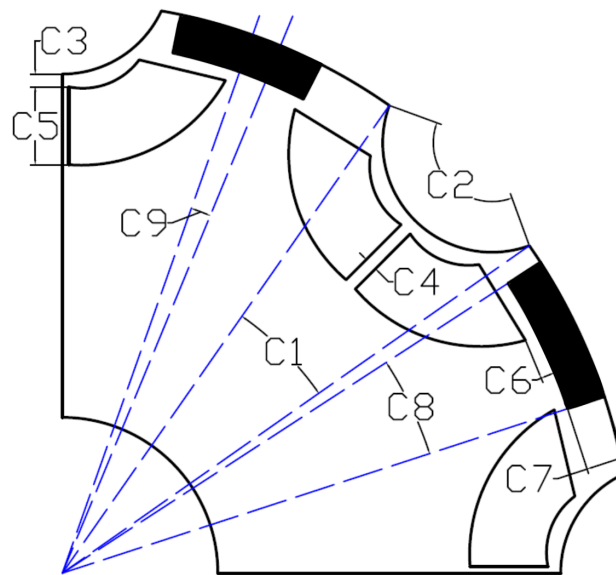


Figure 6. Design variables of case C.

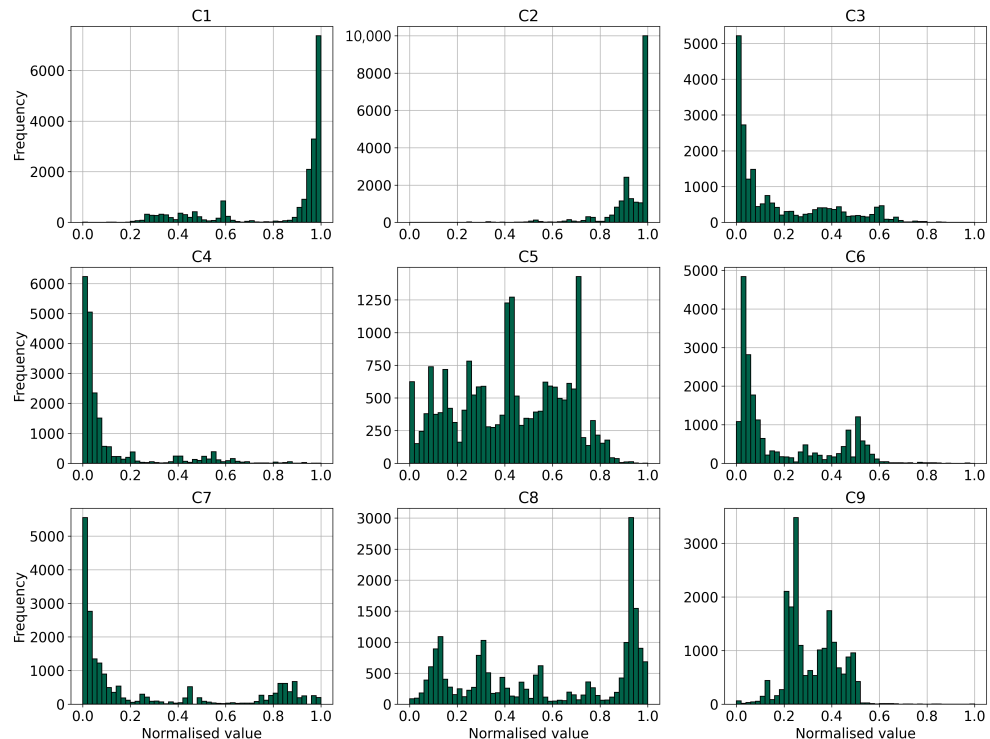


Figure 7. Distribution of the design variables based on the NSGA-II optimisation history of case C.

2.1.4. Case D with PM and MFB Shifting Plus with MFB Extension

Case D (Figure 8) extends case C by introducing design variable D_{10} , i.e., the width of the MFB, which creates lateral air barriers adjacent to the inset PMs (not to be confused with the machine air gap). Together with the PM shifting angle (D_9), this topology combines PM displacement with an extended MFB: when $D_9 \neq 0$, the two air barriers have equal widths because the PM is shifted with the MFB; if $D_9 = 0$, the air barriers are symmetric about the d -axis. Figure 9 shows the normalised distribution of the design variables: on the x -axis, 0 denotes the lower bound and 1 is the upper bound; the y -axis indicates the frequency of occurrence in the optimisation history.

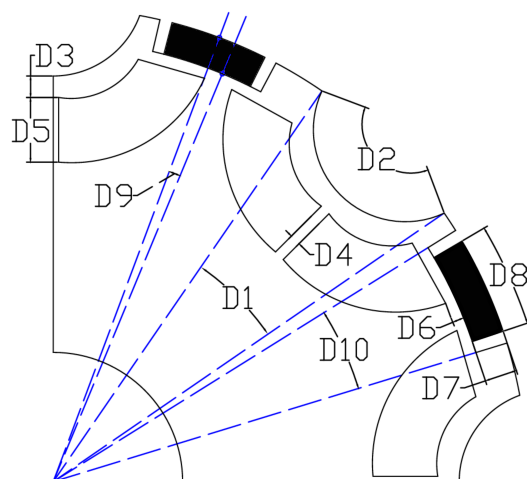


Figure 8. Design variables of case D.

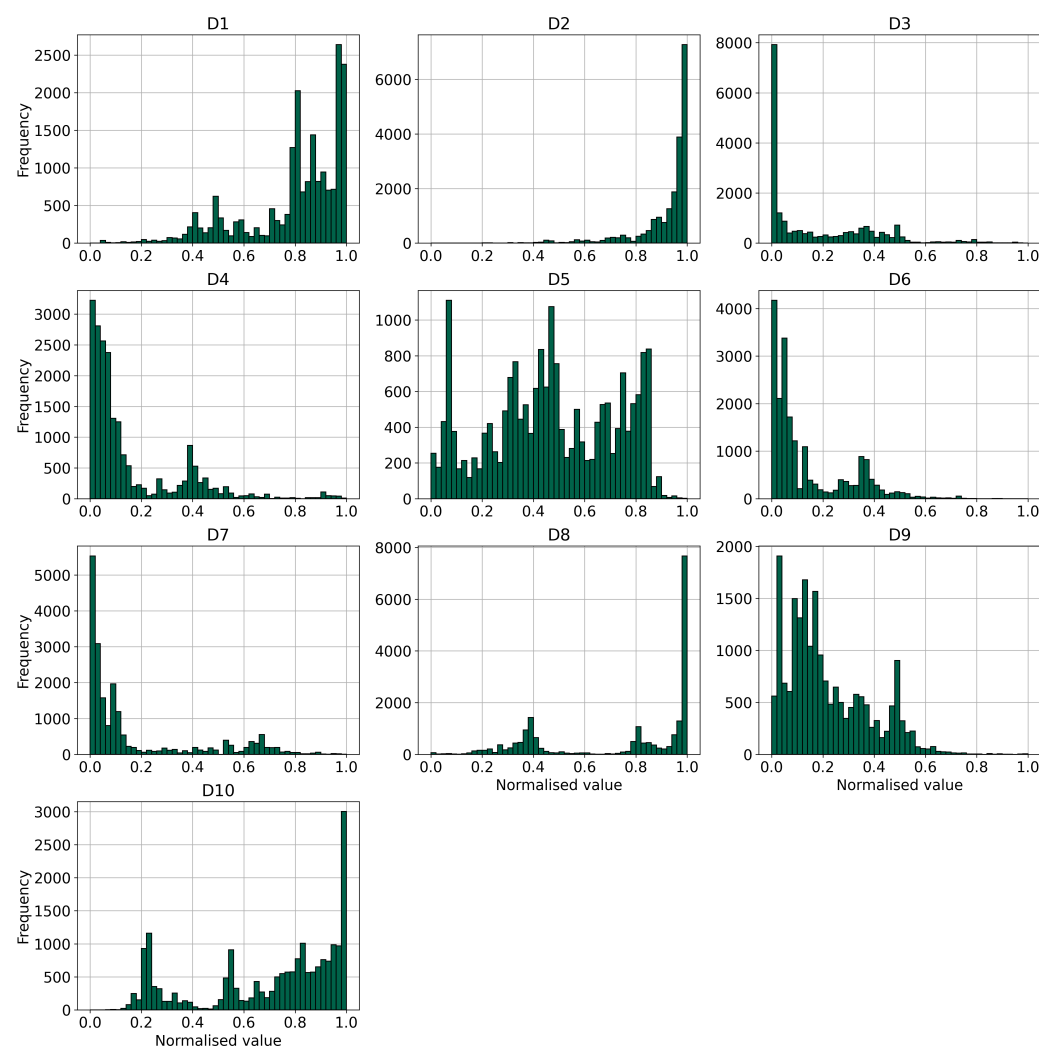


Figure 9. Distribution of the design variables based on the NSGA-II optimisation history of case D.

As all NSGA-II runs were initialised with the same random seed, differences relative to case A reflect the influence of two additional degrees of freedom (D_9 and D_{10}), so shifts in the shared variables (X_1 – X_8) cannot be uniquely attributed to a single factor. Relative to case C, only one new degree of freedom is added (D_{10}): the distributions are broadly similar, with the PM shifting angle (D_9) tending towards lower values, consistent with

the reduced free width introduced by the extended MFB. The implications for torque are discussed in Section 3.

2.2. Data Processing and Similarity Metrics

The NSGA-II optimisation history stores torque-related outputs in two files per model: (i) loaded runs yielding average torque and torque ripple and (ii) zero-current runs for cogging-torque evaluation, which require separate FEA simulations. Therefore, the first consolidation step is to join these results. Missing data must be handled explicitly: for some models, the average torque is available while the cogging torque run fails (e.g., due to a timeout) and vice versa. The outcome is a single, consolidated optimisation-history dataset, as outlined in the process diagrams of Figures 10 and 11. For cross-case comparison, direct one-to-one matching of items between cases A–D by raw design variables is not guaranteed because NSGA-II selection and mutation do not ensure identical designs across runs. Thus, a similarity metric is introduced over the shared design variables to enable meaningful pairing and aggregation. In this work, the baseline metric is the normalised Euclidean distance, i.e.,

$$\delta(i, j) = \sqrt{\sum_{k \in S} \left(\frac{x_k^{(i)} - x_k^{(j)}}{\Delta x_k} \right)^2},$$

where S is the set of shared variables and Δx_k is the optimisation-range width of variable k . Advantages and limitations of alternative metrics are summarised in Table 2. As cosine similarity is effective for textual data, the Manhattan distance is suited for grid-based movements and Jaccard similarity targets binary or categorical data; none of these align with the aim of this study. Minkowski distance reduces to the Manhattan distance for $p = 1$ and Euclidean distance for $p = 2$ but becomes less interpretable for non-standard p values. Mahalanobis distance accounts for feature correlations but requires the estimation of the covariance matrix, which can be computationally costly. Random Forest similarity likewise entails substantial computational overhead due to model training. Considering these trade-offs, we adopt an Euclidean distance-based similarity for the present investigation.

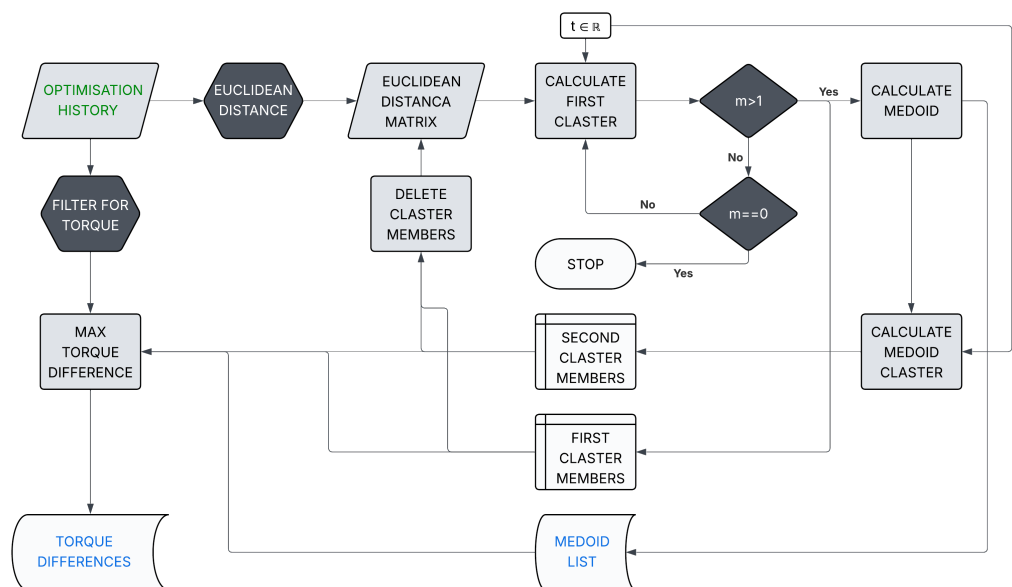


Figure 10. Process chart for similarity matrix-based filtering.

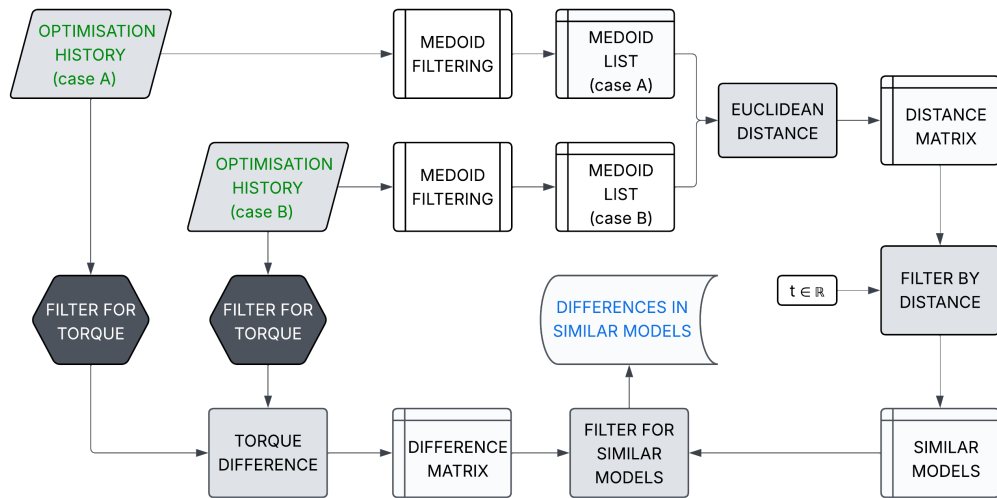


Figure 11. Process chart for similarity matrix-based comparison.

Element-wise comparisons between case A and case B (or other cases), filtered by an Euclidean distance-based similarity, can be used to present torque differences. However, if models within a case are not first filtered to enforce dissimilarity, the results may be distorted. To ensure that models in case A (and in other cases) are mutually dissimilar, we introduce a filtering step that yields a dataset in which all models are at least t_f apart in Euclidean distance. A filtering algorithm was developed to enforce non-similarity, inspired by clustering methods such as K-Medoids [27] and DBSCAN [28]. The objectives are (i) for no pair of models to be closer than t_f in Euclidean distance and (ii) for each cluster to be represented by its medoid to minimise information loss.

K-Medoids is a partitioning technique that selects the most centrally located object (the medoid) as the cluster representative, rather than the mean as in K-Means. This makes it less sensitive to noise and outliers and often yields better spatial clustering quality than K-Means. However, K-Medoids is computationally demanding [27], and its primary input is the number of clusters (k) rather than a minimum separation threshold. In contrast, DBSCAN identifies clusters as high-density regions separated by sparser areas using two inputs: the neighbourhood radius (ϵ) and the minimum number of points $minPts$ [28]. DBSCAN, however, does not provide medoids.

Because K-Medoids is computationally intensive and does not directly enforce a minimum pairwise distance and DBSCAN does not yield medoids, we developed the following procedure (illustrated in Figures 10 and 11) to ensure that models within a case are not similar. Any two models closer than t_f in Euclidean distance are deemed similar.

In-case filtering subprocess (Figure 10). Starting from the optimisation history of case A, we construct the pairwise Euclidean distance matrix as

$$D_{ij} = \|x_i - x_j\|_2,$$

where x_i denotes the design-variable vector of model i . To initialise the first cluster, the algorithm selects the last computed model of the NSGA-II run (denoted m_i), i.e., the last column of D . Owing to NSGA-II elitism, models computed later are more likely to be closer to the Pareto front; prioritising them helps retain information about non-dominated solutions. If no models lie within t_f of m_i , then m_i is appended to the medoid list. Otherwise, a cluster is formed from all models within t_f of m_i , its medoid is computed and appended to the medoid list and all cluster members are removed. Subsequently, any remaining models within t_f of the chosen medoid are also removed. For each cluster, we compute

quality measures—maximum differences in average torque, torque ripple, and cogging torque—between each member and the medoid. The subprocess iterates until no models remain and is repeated for multiple t_f values to enable selection of the best threshold according to the quality metric.

Table 2. Comparison of similarity metrics: working principles, advantages, and disadvantages.

Method	Working Principle	Advantages	Disadvantages	Usage
Euclidean Distance	Calculates straight-line distance between two points in n-dimensional space, called the L2 norm.	Simple to understand and implement; computationally efficient; works well for continuous numerical data.	Sensitive to feature scaling and high-dimensional data. It may not capture complex relationships.	Adaptive Pareto algorithm optimisation [29], fault diagnosis [30], and clustering [31]
Cosine Similarity	Measures the cosine of the angle between two vectors; it focuses on orientation.	Scale-invariant; excellent for high-dimensional, sparse data like text; captures semantic similarity.	Ignores magnitude information; can be misleading with negative values.	Fault diagnosis [32] and keyword extraction [33]
Manhattan Distance	The distance between two vectors equals the L1 norm of their difference, i.e., $\ x - y\ _1 = \sum_i x_i - y_i $.	Computationally simple, effective with categorical/sparse data, and optimal for grid-based movements.	Poor at capturing diagonal relationships; assumes all features are equally important.	Used in fault diagnosis [34] and excitation current prediction for reactive power compensation [35]
Jaccard Distance	Dissimilarity defined as $1 - J(A, B)$.	Shares the same strengths as Jaccard similarity for sparse, binary data.	Same limitations: unsuitable for continuous features; only exact matches.	Detection of hotspots in thermal imaging [36] and CAN bus attack detection [37]
Minkowski Distance	Generalized distance metric defined as $\ x - y\ _p = (\sum_{i=1}^n x_i - y_i ^p)^{1/p}$, where p is the order parameter.	Flexible framework that unifies several norms (e.g., $p = 1 \rightarrow$ Manhattan, $p = 2 \rightarrow$ Euclidean); tunable for specific applications.	Choice of p can be challenging and may reduce interpretability for non-standard values.	Applied in acoustic signal recognition [38] and demagnetisation fault diagnosis [39]
Mahalanobis Distance	Distance that accounts for variable correlations via the covariance matrix: $d_M(x, y) = \sqrt{(z)^T \Sigma^{-1}(z)}$, where $z = (x-y)$.	Incorporates feature correlations and scale; effective for multivariate outlier detection and anomaly scoring.	Requires reliable covariance estimation; sensitive to small samples and multicollinearity; can be computationally costly.	Applied to fault diagnosis of electric motors using uniaxial acceleration signals [40]
Random Forest Similarity	Similarity between samples defined by their co-occurrence in leaf nodes across trees of a trained random forest.	Captures complex non-linear relationships, robust to noise and missing data, and naturally leverages ensemble learning.	Computationally intensive for large datasets and dependent on the training of a random forest model; similarity is model-specific and may lack interpretability.	Applied to early fault detection in semiconductor manufacturing [41]

The resulting dataset records for each tested t_f include the following: the number of medoids; the mean and maximum of maximum differences in average torque, torque ripple, and cogging torque (relative to each cluster's medoid) over all clusters; and the indices of the medoids. This ensures that, within any case, all retained models are at least

t_f apart in Euclidean distance. The t_f threshold is selected per case based on these quality metrics (see Section 3), and the resulting medoids are then passed to the comparison stage.

Comparison subprocess (Figure 11). Ensuring that the Euclidean distance between any models in two cases is at least t_c , thereby ensuring similarity, a comparison subprocess is used. The Euclidean distances between two models of the two cases are determined based on similar design variables, ensuring comparability and isolating the effect of the design variable, which is only present in one of the two cases being compared.

This approach enables the possibility of more than one model from case B being similar to case A, despite two models in one case not being similar to each other. An example in Equations (1)–(3) shows the possibility in lower dimensions. In the equations, x , y , and z denote design variables, where x represents the height of the IFB, y represents the width of the PM, and z represents the width of the MFB. A_i and A_j denote the i^{th} and j^{th} models in case A. The Euclidean distance between two models of case A (d_{AA}) is ensured by setting the filtering subprocess to be lower than the t_f threshold, similar to case B of Equation (2). In the comparison process, case A and case B can only be compared based on their similar design variables, i.e., x and y . In the case of Equation (3), design variable z is neglected, which makes it possible that B_i and B_j are similar in the x and y dimensions but differ in the x , y , and z dimensions. Therefore, B_i and B_j may be both similar to A_i in the x and y dimensions. For the purpose of this paper, this is not a limitation but a plus, as the variation in the isolated design variable provides additional information.

$$d_{AA} = \sqrt{(x_{Aj} - x_{Ai}) + (y_{Aj} - y_{Ai})} < t_{fA} \quad (1)$$

$$d_{BB} = \sqrt{(x_{Bj} - x_{Bi}) + (y_{Bj} - y_{Bi}) + (z_{Bj} - z_{Bi})} < t_{fB} \quad (2)$$

$$d_{BA} = \sqrt{(x_{Bi} - x_{Ai}) + (y_{Bi} - y_{Ai})} < t_c \quad (3)$$

Table 1 highlights the fact that the different design variables are measured in different units. To address this comparability issue of varying measurement units, all design variables were normalised to a range of 0 to 1 using Equation (4). One example of the similarity matrix is presented in Table 3.

$$x_{scaled,i,j} = \frac{(x_{i,j} - x_{i,min})}{(x_{i,max} - x_{i,min})} \text{ where } i \in [X_1 \dots X_n]; \quad X \in [A, B, C, D]; \quad j \in [0 \dots m] \quad (4)$$

Table 3. Filtered similarity matrix based on the Euclidean distance between case A and case B.

	0	1	2	4	...	20,032	20,036	20,047	20,050
1	0.740	0.647	1.079	1.587	...	1.037	1.188	0.984	1.055
2	0.764	0.926	1.071	1.102	...	0.611	0.668	0.782	0.986
3	0.720	1.084	0.849	1.260	...	1.066	1.328	0.708	0.973
4	0.992	1.180	1.288	1.118	...	1.034	1.178	0.853	1.366
5	1.275	1.498	0.891	1.130	...	1.787	1.984	1.486	1.684
:	:	:	:	:	:	:	:	:	:
18,093	0.686	0.953	0.939	1.531	...	0.871	1.172	0.379	0.709
18,094	0.891	1.094	1.146	1.480	...	0.462	0.484	0.946	0.643
18,100	0.595	0.885	0.894	1.605	...	0.844	1.017	0.750	0.168
18,103	1.147	1.437	1.428	1.431	...	0.446	0.167	1.213	1.084
18,104	0.834	1.159	1.104	1.382	...	0.764	1.012	0.474	0.879

Once all the distances between the models are determined, a minimum acceptable distance (t_c) is defined. If the actual distance is lower than or equal to t_c , the models are deemed similar. For this investigation, $t_c = 0.05$ was chosen, as it promotes similarity in the manufacturing tolerance range. Plus, $t_c = 0.05$ ensures a comparison where there is no design-variable collision in the comparison of case C and case D, as shown in Figure 12a,b. The presented comparison is between the C_8 (width of the PM) and D_{10} (width of the MFB), meaning if $t_c = 0.06$, as shown in Figure 12a, the difference between the inset PM and its place in the rotor can be negative, so the PM does not fit into its place, which is a violation of feasibility. At $t_c = 0.05$, as shown in Figure 12b, this is not the case. In the case of other comparisons between case A and case B or between case A and case C, there is no variable collision observable at $t_c = 0.05$ in this dataset.

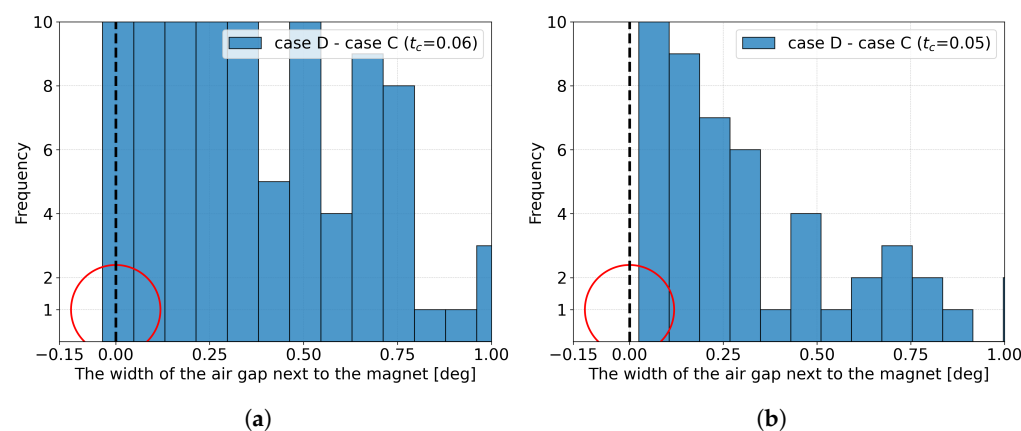


Figure 12. Design-variable collision at (a) $t_c = 0.06$ and a feasible comparison at (b) $t_c = 0.05$ between C_8 (width of the PM) and D_{10} (width of the MFB).

As mentioned beforehand, the precision of the design variables in the NSGA-II optimisation is 0.01, which is below the reasonable manufacturing tolerance range for the investigated design variables but enables similarity in the manufacturing tolerance range. One possible difference between the models at $t_c = 0.05$ is summarised in Table 4 for each design variable converted to its original unit, where the maximum difference occurs when all parameters have identical values except for one. The last column highlights the differences in the design variables of the two compared models, given the specified Euclidean distance weights.

As the differences are sufficiently small, the effects of the similar design variables can be neglected, allowing the comparison to effectively highlight the differences in torque related to the air barrier adjacent to the PMs and PM displacement. The comparisons of average torque, torque ripple, and cogging torque between cases A and B, cases A and C, cases C and D, and cases A and D, plus the width of the air gap between cases A and B and cases C and D, were conducted with a similar methodology. First, given an objective function such as the cogging torque for two cases, all model pairs were subtracted from each other in a similar matrix format, as in the Euclidean similarity matrix, referred to as the difference matrix. This makes it possible to filter the Euclidean similarity matrix for model pairs where the distance (t_c) is lower than or equal to $t_c = 0.05$ and list out all (row (r), column (c)) pairs. The rc pairs are used to filter the difference matrix and list out all results. Checking of the air barrier next to the PMs follows a similar methodology, as shown in Figure 11, but with the corresponding design variables. In summary, a one-to-one comparison is not possible based on the NSGA-II optimisation history; nonetheless, the models differ only by one design variable and have the same optimisation ranges. One potential solution is a similarity matrix-based comparison, as described in this section.

Table 4. The maximum difference that can occur for a design variable if the Euclidean distance between two models is less than 0.05, where Eucl. Dist. Weight refers to the Euclidean distance weight, which represents the possible element-wise distance between the two models. The precision of the optimisation is reported to two decimal places.

Variables	Maximum Difference	Eucl. Dist. Weight	Difference
A_1, B_1, C_1, D_1	0.5 deg	0.06	± 0.17 deg
A_2, B_2, C_2, D_2	3.24 deg	0.001	± 0.05 deg
A_3, B_3, C_3, D_3	0.16 mm	0.013	± 0.06 mm
A_4, B_4, C_4, D_4	0.05 mm	0.014	± 0.09 mm
A_5, B_5, C_5, D_5	0.18 mm	0.019	± 0.04 mm
A_6, B_6, C_6, D_6	0.04 mm	0.02	± 0.01 mm
A_7, B_7, C_7, D_7	0.02 mm	0.033	± 0.01 mm
A_8, B_8, C_8, D_8	0.25 mm	0.016	± 0.08 mm
B_9, D_{10}	0.35 deg	-	-
C_9, D_9	0.39 deg	-	-

3. Results and Discussion

3.1. Comparison of Case A and Case B

The first step in the comparison is to determine the value of the in-case filtering threshold (t_f), which can be calculated using the result of the filtering subprocess presented in Figures 13 and 14. The optimal filtering threshold is chosen using the in-cluster torque differences as quality measures. In the whole dataset of case A, the average torque ranges from 665.6 mNm to 2043.5 mNm, the torque ripple ranges from 14.18% to 131.8%, and the cogging torque ranges from 18.13 mNm to 21.87 mNm. At the $t_{fA} = 0.07$ threshold, the in-cluster average torque difference is 37.204 mNm, its maximal outlier is 173.617 mNm, the in-cluster torque ripple difference is 3.293%, its maximal outlier is 19.054%, the in-cluster cogging torque difference is 0.359 mNm, and its maximal outlier is 1.500 mNm. The dataset is reduced to 7029 models. Considering that this paper focuses on cogging torque, this difference is acceptable.

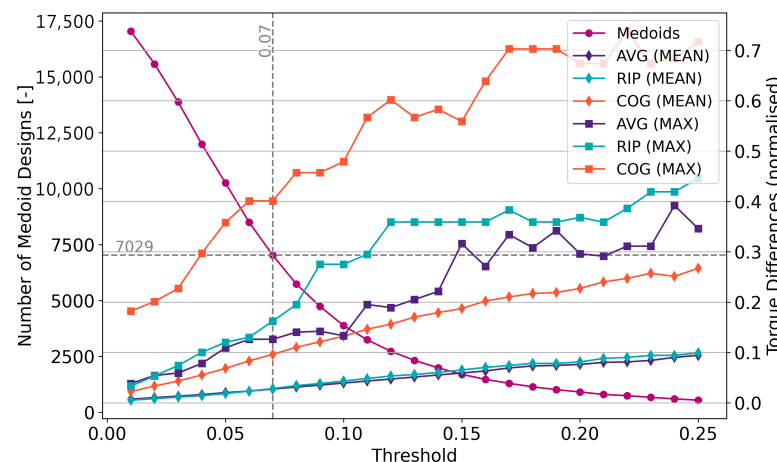


Figure 13. The results of the filtering subprocess for case A representing the number of medoid designs and normalised torque differences against different threshold values.

In the whole dataset of case B, the average torque ranges from 593.5 mNm to 2013.8 mNm, the torque ripple ranges from 2.9% to 158.9%, and the cogging torque ranges

from 13.38 mNm to 22.20 mNm. At the $t_{fB} = 0.07$ threshold, the in-cluster average torque difference is 32.666 mNm, its maximal outlier is 153.387 mNm, the in-cluster torque ripple difference is 2.965%, and its maximal outlier is 23.717%. The in-cluster cogging torque difference is 0.353 mNm, with a maximal outlier of 2.090 mNm. The dataset is reduced to 9495 models. Considering that this paper focuses on cogging torque, this difference is acceptable.

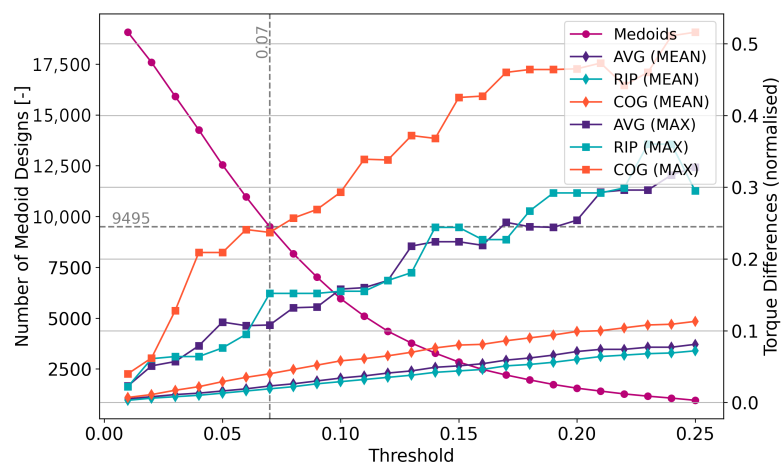


Figure 14. The results of the filtering subprocess for case B, representing the number of medoid designs and normalised torque differences against different threshold values.

In terms of average torque comparison (shown in Figure 15a) and torque ripple comparison (shown in Figure 15b), there is no clear conclusion as to whether the presence of the isolated design variable in similar models decreases or increases the torque values. The figures present the sorted torque differences and the comparison indexes. On the other hand, in terms of cogging torque (shown in Figure 16a), the presence of a 0.5- to 4-degree gap (shown in Figure 16b) between the surface-inset PM and the rotor steel body decreases it by 0 to -5.7 mNm in 70.7% of all the similar models.

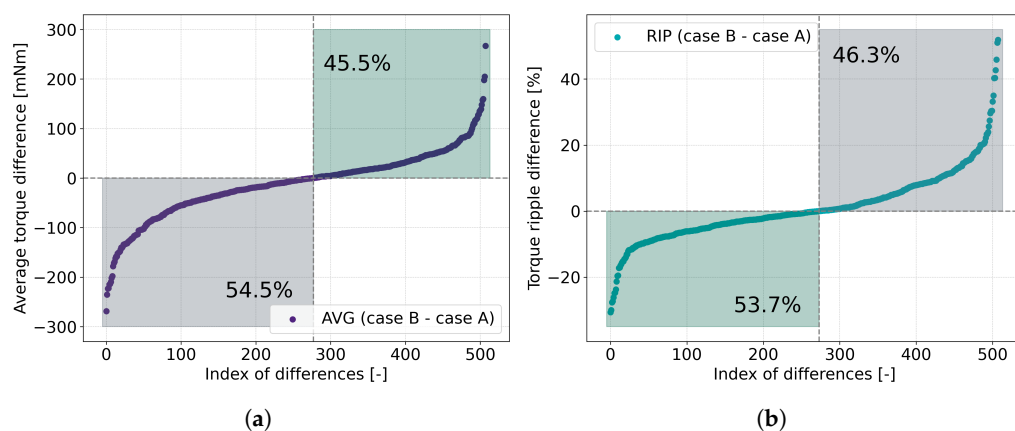


Figure 15. Differences in (a) average torque and (b) torque ripple between case A and case B.

In the comparison of case A—with no PM displacement or air barriers next to the PMs—and case B—with no PM displacement and air barriers next to the PMs—a 0 mNm to ± 300 mNm difference can be seen in the average torque (shown in Figure 15a) with 54.5% and 45.5% distributions. In terms of torque ripple (shown in Figure 15b), a 0% to -25% difference with 53.7% proportion and a 0% to 45% difference with 46.3% is present in the comparison. In conclusion, the presence of air barriers next to the PMs does not

improve or diminish the average torque and torque ripple in an explicit way. However, the cogging torque (shown in Figure 16a) is decreased between 0 mNm and -5.7 mNm with a proportion of 70.7% against only a 0 mNm to 2.4 mNm possible torque increase with a proportion of 29.3%. The results suggest that the presence of air barriers adjacent to the PMs, without PM displacement, tends to reduce the cogging torque in most cases.

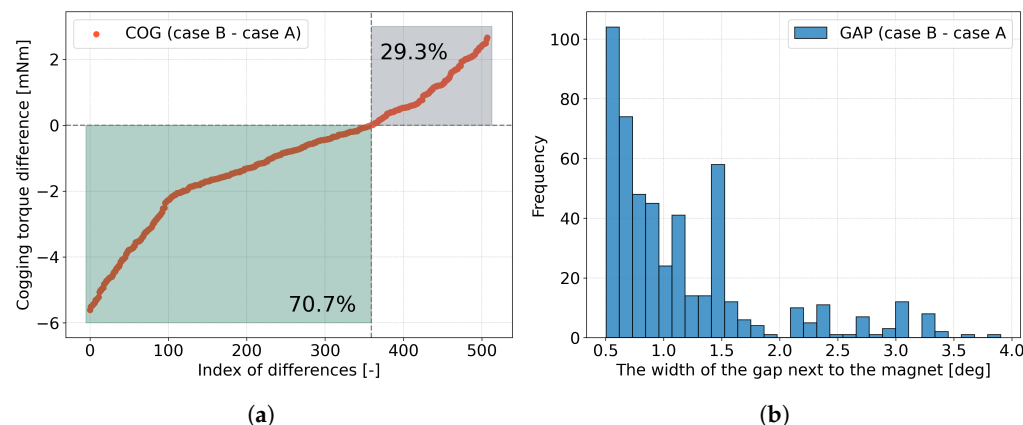


Figure 16. Differences in (a) cogging torque and (b) the width of the air barrier next to the PM between case A and case B.

3.2. Comparison of Case A and Case C

In the whole dataset of case C, the average torque ranges from 693.1 mNm to 2253.2 mNm, the torque ripple ranges from 8.3% to 128.1%, and the cogging torque ranged from 18.02 mNm to 22.04 mNm. At the $t_{fC} = 0.05$ threshold (Figure 17), the in-cluster average torque difference is 26.523 mNm, its maximal outlier is 146.656 mNm, the in-cluster torque ripple difference is 2.036%, its maximal outlier is 22.872%, the in-cluster cogging torque difference is 0.382 mNm, and its maximal outlier is 2.340 mNm. The dataset is reduced to 13,835 models. Considering that this paper focuses on cogging torque, this difference is acceptable.

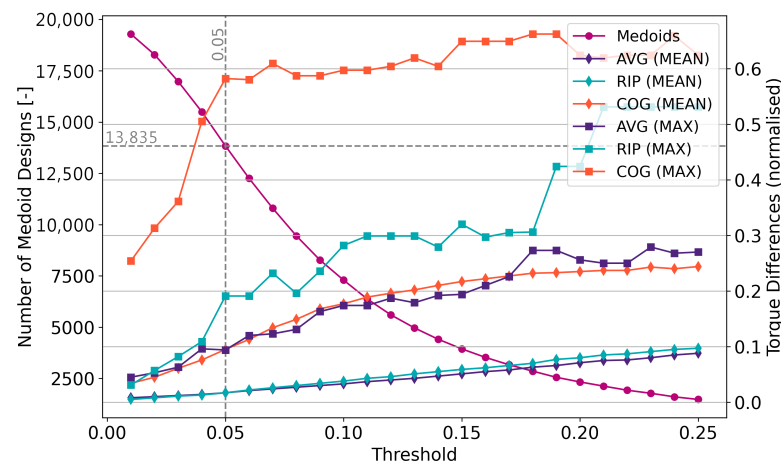


Figure 17. The results of the filtering subprocess for case C, representing the number of medoid designs and normalised torque differences against different threshold values.

In the comparison of case A—with no PM displacement or air barriers next to the PMs—and case C—with PM displacement and no air barriers next to the PMs—a significant 0 mNm to -700 mNm difference can be seen in the average torque (shown in Figure 18a), with a 70.3% proportion, considering the outliers. In terms of torque ripple (shown in

Figure 18b), a significant 0% to -35% difference with a 77.5% proportion is present in the comparison. In conclusion, the presence of PM displacement improves the torque ripple but diminishes the average torque. However, the cogging torque (shown in Figure 19a) tends to increase between 0 mNm and 2.1 mNm with a proportion of 62.1%.

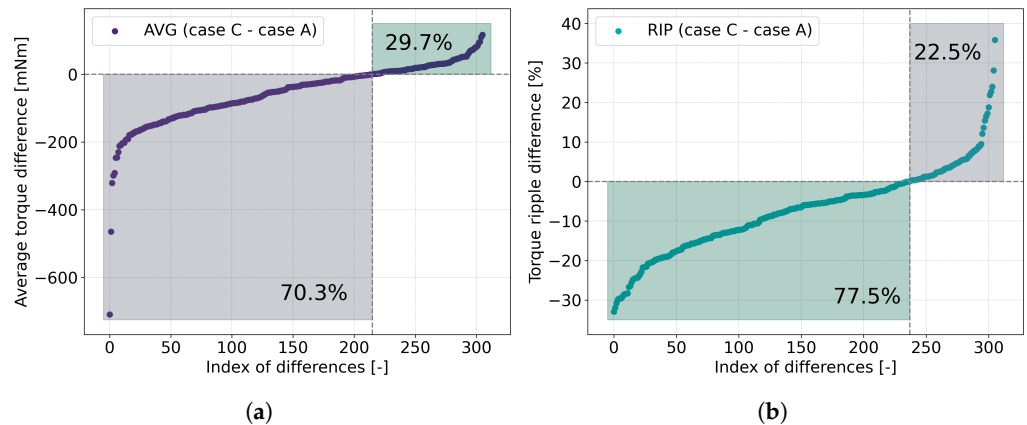


Figure 18. Differences in (a) average torque and (b) torque ripple between case A and case C.

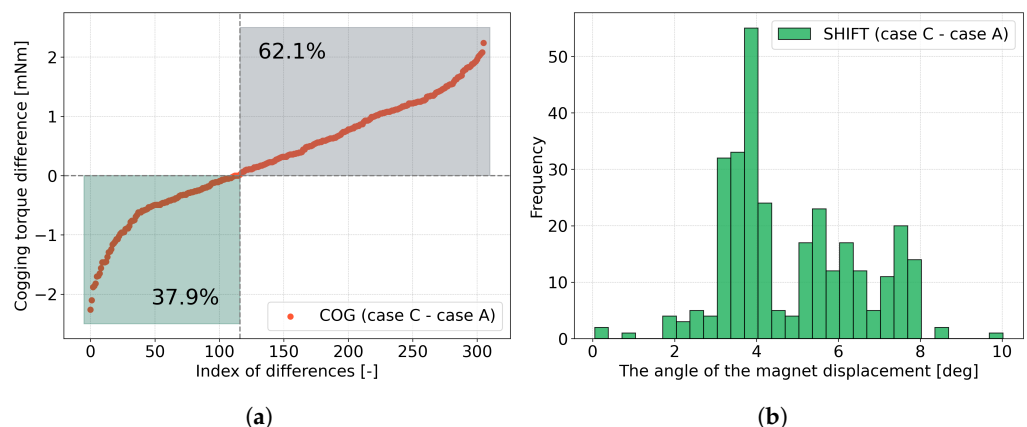


Figure 19. Differences in (a) cogging torque (b) and angle of PM shift between case A and case C.

3.3. Comparison of Case C and Case D

In the whole dataset of case D, the average torque ranges from 932.2 mNm to 2184.9 mNm, the torque ripple ranges from 3.96% to 122.3%, and the cogging torque ranges from 12.99 mNm to 22.18 mNm. At the $t_{fD} = 0.07$ threshold (Figure 20), the in-cluster average torque difference is 26.307 mNm, its maximal outlier is 129.031 mNm, the in-cluster torque ripple difference is 2.012%, its maximal outlier is 13.374%, the in-cluster cogging torque difference is 2.702 mNm, and its maximal outlier is 8.583 mNm. The dataset is reduced to 13,433 models.

In terms of cogging torque, the average of the maximal differences relative to the medoid is higher than in the previous cases, which is in line with the findings of an earlier study [7]. From there, the results of the sensitivity analysis showed that, in unidirectional PM displacement with air barriers, the width of the PM, the width of the MFB, the shifting angle of the PM, and the shifting angle of the MFB have the most significant effect on the cogging torque. Thus, by introducing all these design variables, there is a possibility that, in addition to the near-exact similarity between D_1 and D_6 , the in-threshold difference between D_7 and D_{10} could significantly affect the cogging torque, suggesting high sensitivity.

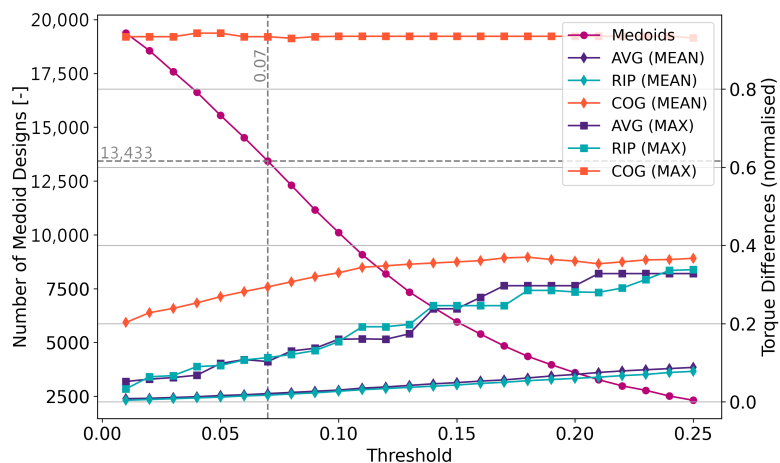


Figure 20. The results of the filtering subprocess for case D, representing the number of medoid designs and normalised torque differences against different threshold values.

In the comparison of case C—with PM displacement and no air barriers next to the PMs—and case D—with PM displacement and air barriers next to the PMs—the only difference between the design variables, i.e., rotor configurations, is the presence of an air barrier, as both contain PM displacement. Therefore, the results are similar in nature to the comparison of case A with case B. A difference of approximately 0 mNm to ± 100 mNm difference can be seen in the average torque (shown in Figure 21a) with 62.5% and 37.5% distributions. In terms of torque ripple (shown in Figure 21b), a 0% to -15% difference with a 41.1% proportion and a 0% to 10% difference with a 58.9% proportion are present in the comparison. However, the cogging torque (shown in Figure 22a) is decreased between 0 mNm and -6.9 mNm with a proportion of 67.9% against only 0 mNm to a 2.1 mNm possible cogging torque increase with a proportion of 32.1%. The results suggest that the presence of air barriers adjacent to the PMs, with PM displacement, also tends to reduce the cogging torque significantly in most cases.

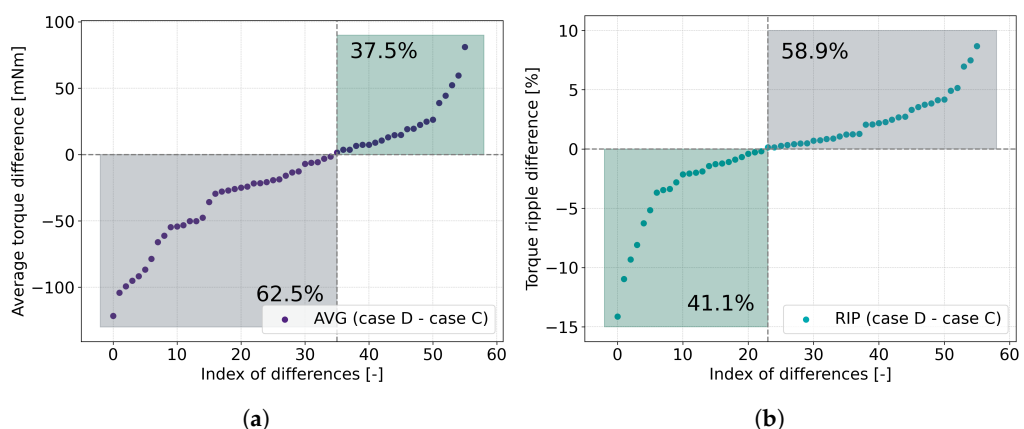


Figure 21. Differences in (a) average torque and (b) torque ripple between case C and case D.

3.4. Comparison of Case A and Case D

As a combined effect of both PM displacement and air barriers, the comparison of case A and case D shows that, generally, a significant torque-ripple reduction (shown in Figure 23b) can be achieved in a range between 0% and -58% with a proportion of 82.3% of all similar cases. Similarly, a 0 mNm to -7.8 mNm reduction in cogging torque (shown in Figure 24a) is possible in 79.6% of all similar cases. While reducing torque ripple and cogging torque is desirable, it also comes with the disadvantage of reducing average torque

output (shown in Figure 23a) in a range between 0 mNm and -382 mNm (ignoring the outlier) at 62.3% of all similar cases.

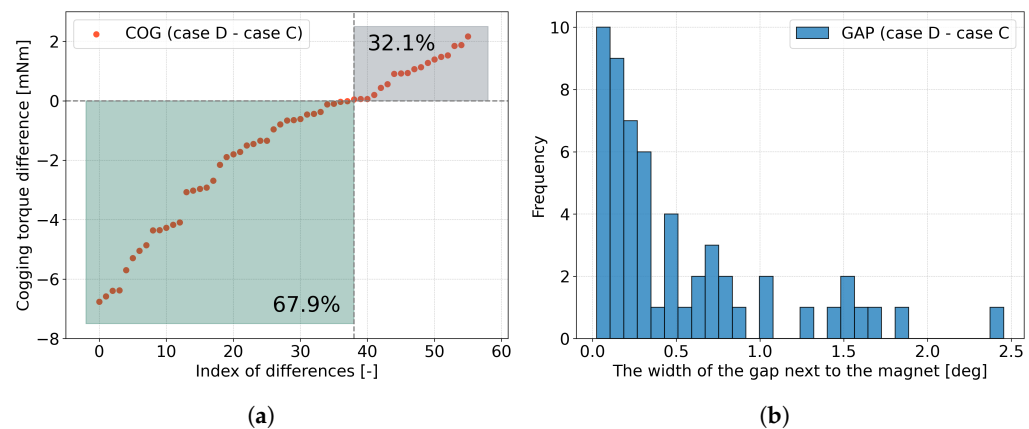


Figure 22. Differences in (a) cogging torque and (b) the width of the air barrier next to the PM between case C and case D.

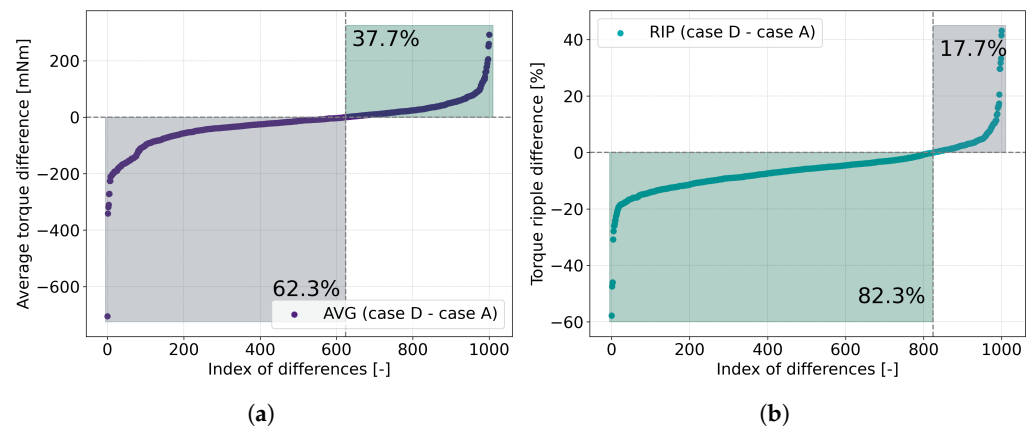


Figure 23. Differences in (a) average torque and (b) torque ripple between case A and case D.

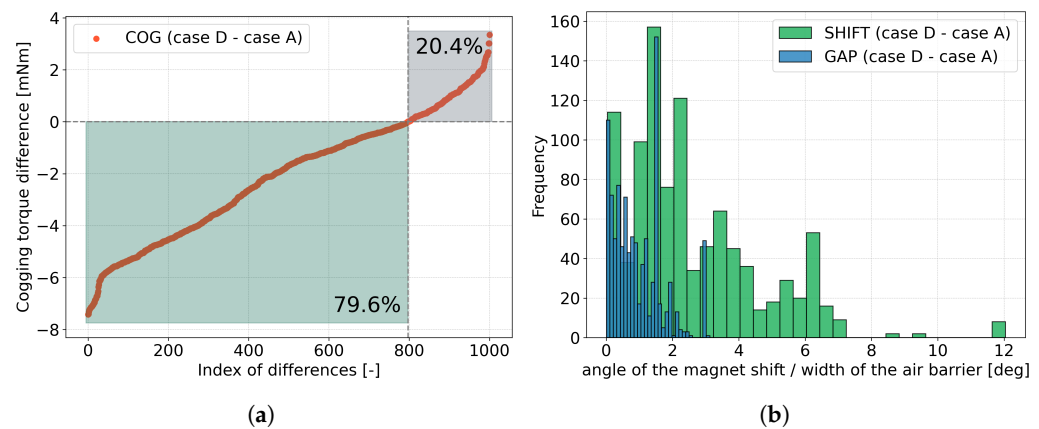


Figure 24. Differences in (a) cogging torque and (b) angle of PM displacement, plus the width of the air barrier next to the PM, between case A and case D.

The results show that introducing only unidirectional displacement for all PMs simultaneously (case C), relative to the base configuration (case A), does not reduce cogging torque in most comparable cases; however, when air barriers are also introduced (case D), both torque ripple and cogging torque are reduced, while the average torque is possibly

maintained. In the following one particular model ($X1: 20^\circ$, $X2: 13^\circ$, $X3: 0.5 \text{ mm}$, $X4: 0.5 \text{ mm}$, $X5: 3 \text{ mm}$, $X6: 1 \text{ mm}$, $X7: 1.5 \text{ mm}$, $X8: 15^\circ$, $B9: 17^\circ$ ($X \in [A, B]$)) is presented as an example to show the peak cogging-torque reduction with MFB extension, which is a significant 20%. The mechanism leading to the reduction is depicted in Figure 25a,b, which show the tangential stress component (Equation (5)) of the Maxwell stress tensor in a polar coordinate system of a cylindrical rotor, where $\mu_0 = 4\pi 10^{-7} [\text{H/m}]$ is the vacuum permeability, $B_r [\text{T}]$ is the radial component of magnetic flux density pointing radially across the air gap, and $B_t [\text{T}]$ is the tangential component of magnetic flux density pointing along the circumference of the rotor in the air gap.

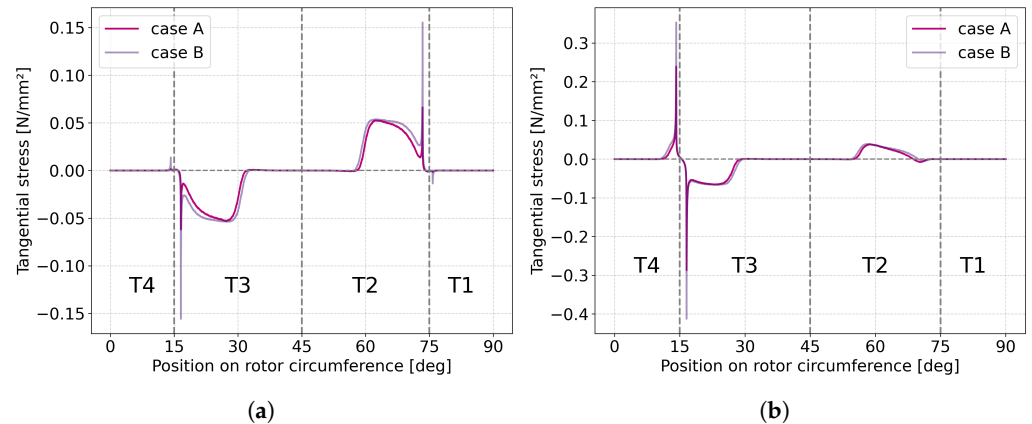


Figure 25. Comparison between one particular model of case A and case B of the tangential stress along the rotor circumference (a) at the rotor position, which corresponds to zero cogging torque, and (b) at the rotor position, which corresponds to maximal cogging torque.

$$p_t = \frac{1}{\mu_0} B_r B_t \quad (5)$$

If the PMs are aligned with the teeth, then the sum of the tangential stress is zero (Figure 25a), which means that the acting forces are purely radial. The sum of the tangential stress becomes non-zero (Figure 25b) when the main flux is asymmetrically distributed, leading to cogging torque. The main flux links the rotor PM and stator teeth across the air gap of the machine. We assume a positive reference direction, so the direction of the rotation is counter-clockwise, which is the direction spanning from 90° to 0° from the *position on the rotor circumference* axis. The flux density is highest near the edges of the teeth; thus, the tangential stress is also highest near the edges of the teeth. Positive tangential stress contributes positively to torque in the chosen rotation direction, while negative tangential stress corresponds to a torque opposing the intended rotation. The tangential forces acting upon the teeth are calculated by Equations (6)–(9), where $r [\text{m}]$ is the air-gap radius, assuming that the air gap is constant; $l [\text{m}]$ is the axial length of the rotor stack, assuming that there is no rotor variation along the shaft; and $\theta [\text{rad}]$ is the angular width of the teeth.

$$F_t^{T4} = r l \int_0^{\pi/12} p_t(\theta) d\theta \quad (6)$$

$$F_t^{T3} = r l \int_{\pi/12}^{\pi/4} p_t(\theta) d\theta \quad (7)$$

$$F_t^{T2} = r l \int_{\pi/4}^{12\pi/5} p_t(\theta) d\theta \quad (8)$$

$$F_t^{T1} = r l \int_{12\pi/5}^{\pi/2} p_t(\theta) d\theta \quad (9)$$

Figure 26a,b compare the absolute values of different forces acting upon the teeth of the investigated model at rotor positions ranging from 0° to 7.5° , which is half of one cogging torque period. The T1 tooth is the first tooth in counter-clockwise rotation, which T2 follows at PM1. The T3 and T4 teeth are connected to PM2 (Figures 27a and 28a). The T1 and T3 teeth exert a force acting in the direction opposite to the rotation, while T2 and T4 act in the direction of the rotation. T1 does not contribute to the cogging torque; the cumulative force of T4 and T2 acts against T3. In case B, where the MFB extension is present, the main flux is higher, leading to higher tangential forces, as well as steeper curves.

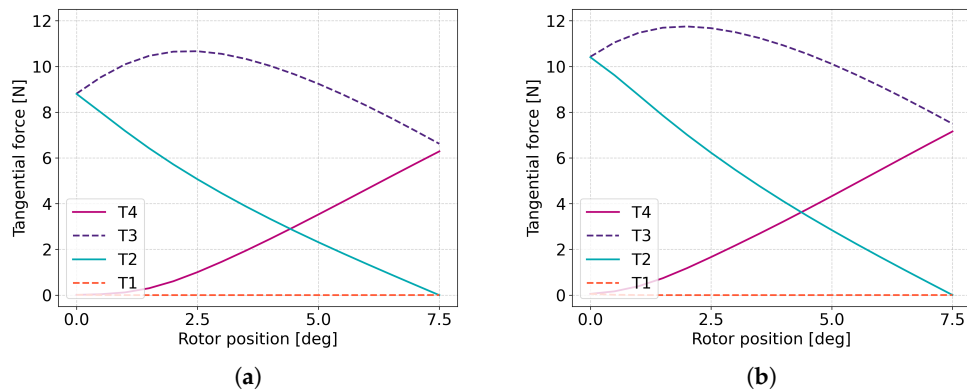


Figure 26. Comparison between one particular model of case A and case B of the forces acting upon the teeth of the machine. (a) case A; (b) case B.

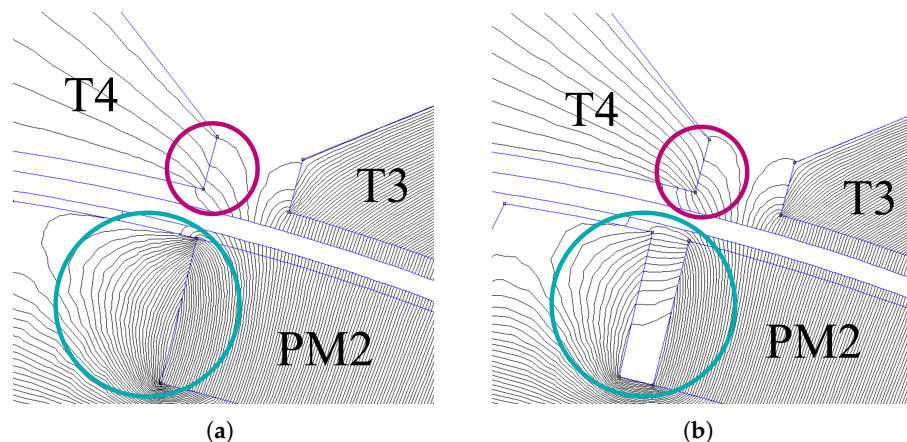


Figure 27. The flux distribution of (a) case A and (b) case B, highlighting the effect of MFB extension on flux lines, where the blue circle corresponds to leakage flux and the purple circle corresponds to the main flux connecting to T4 tooth.

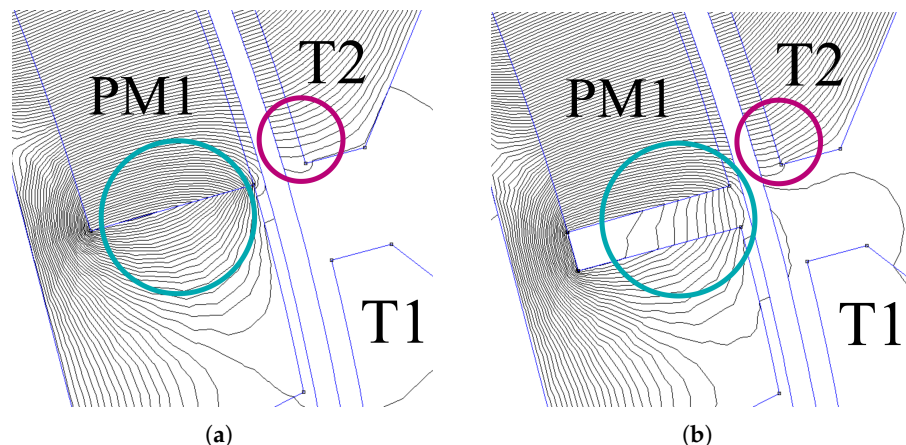


Figure 28. The flux distribution of (a) case A and (b) case B, highlighting the effect of MFB extension on flux lines, where the blue circle corresponds to leakage flux and the purple circle corresponds to the main flux connecting to tooth T2.

The effect of steeper curves is shown in Figure 29a,b—namely, the absolute values of the cumulative forces acting in the direction of rotation ($T_4 + T_2$) and in the opposite direction ($T_3 + T_1$). In case B, where the MFB extension is present, the forces in either direction are higher; however, the area between the two curves, i.e., the difference between the forces, is smaller, which leads to lower cogging torque.

The magnetic flux naturally takes the path of least reluctance through the steel instead of air. Figures 27a,b and 28a,b show that the leakage flux, which loops back to the PM through nearby air paths or rotor steel without coupling with stator teeth, is significantly reduced in the presence of MFB extension, resulting in a higher main flux. Thus, introducing the MFB extension and an air barrier next to the PM increases the reluctance in the direction of the rotor, forcing connection with the teeth. The effect is similar in the comparison of case C and case D, where PM displacement is present.

The mechanism underlying the 20% cogging-torque reduction (Figure 30a) in the case of the example model is the modification of the reluctance path with MFB extension. The MFB extension leads to lower leakage flux, resulting in a higher main flux. The change in the flux density leads to tangential stress, which generates tangential forces in such a way that the resulting tangential forces (Figure 30b) are lower; nevertheless, the tangential force components acting upon each tooth are higher, leading to lower cogging torque in case B. The mechanism is similar in the comparison of case C and case D.

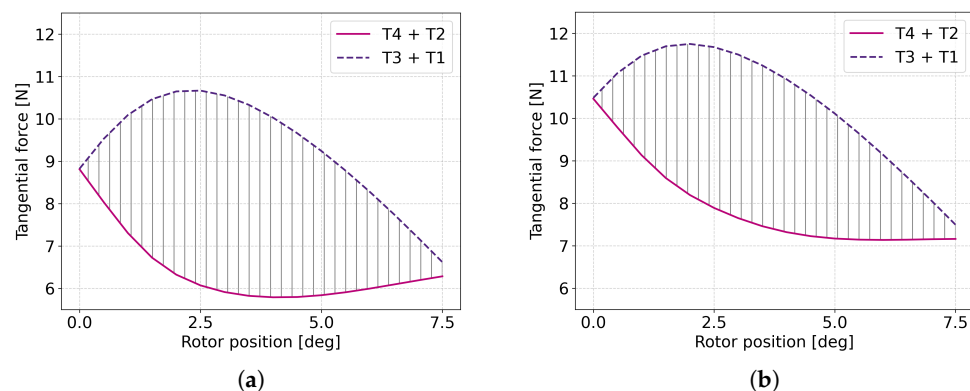


Figure 29. Comparison between one particular model of case A and case B of the forces acting in the direction of rotation or the opposing direction. (a) case A; (b) case B.

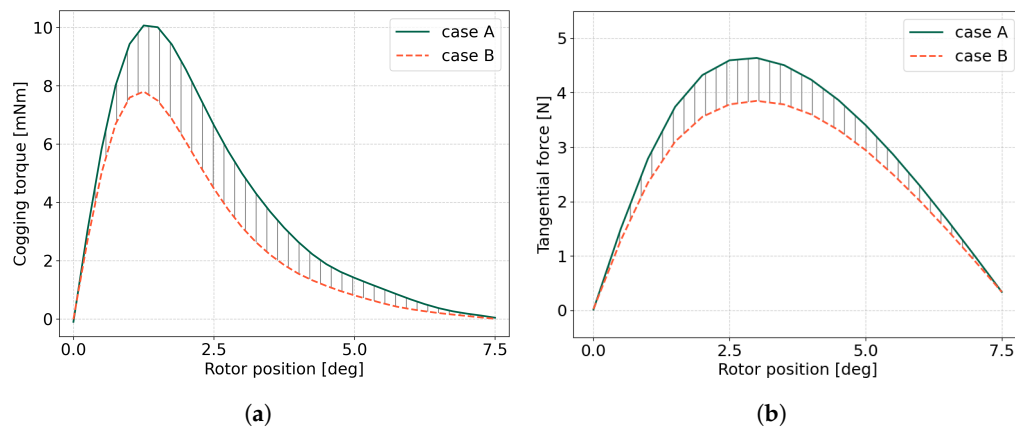


Figure 30. Comparison between one particular model of case A and case B. (a) Cogging torque, highlighting the effect of MFB extension; (b) resulting tangential forces affecting the two poles of the model.

4. Conclusions

This study presents a comparative analysis of four flux-intensifying permanent magnet-assisted synchronous reluctance rotor configurations. The objective is to isolate the effects of (i) permanent magnet (PM) displacement, (ii) air barriers adjacent to the inset magnets, and (iii) their combination on torque components—primarily cogging torque. The dataset for each configuration is the NSGA-II optimisation history. Although element-wise cross-configuration comparisons based on Euclidean similarity can be informative, they can be biased if near-duplicate models are present within a configuration. To mitigate this, we introduce Euclidean distance-based medoid filtering, which ensures any two retained models in a configuration are at least t_f apart. Filtering quality is evaluated using the maximum and mean of the maximum differences in average torque, torque ripple, and cogging torque between cluster members and their medoid. The results indicate that PM displacement alone does not consistently reduce cogging torque; while it markedly lowers torque ripple, it also tends to decrease average torque—an undesirable trade-off. Introducing air barriers alone clearly reduces cogging torque, with mixed effects on average torque and torque ripple. Combining PM displacement with air barriers yields simultaneous reductions in torque ripple and cogging torque. In several configurations, the average torque can be maintained. However, when comparing similar models across configurations, this often comes at the cost of a moderate reduction in average torque. Finally, the leveraging of in-case similarity to identify robust designs emerges as a promising direction for future work.

Author Contributions: Conceptualisation, M.K. and T.O.; methodology, M.K.; investigation, M.K.; resources, M.K. and T.O.; data curation, M.K. and T.O.; writing—original draft preparation, M.K. and T.O.; writing—review and editing, M.K. and T.O.; visualisation, M.K.; supervision, T.O.; funding acquisition, M.K. and T.O. All authors have read and agreed to the published version of the manuscript.

Funding: Project NO. 147030 was implemented with support provided by the National Research, Development, and Innovation Fund of Hungary, financed under the FK funding scheme. Project NO. 2023-2.1.2-KDP-2023-00017 was implemented with the support provided by the Ministry of Culture and Innovation of Hungary from the National Research, Development, and Innovation Fund, financed under the KDP-2023 funding scheme.

Data Availability Statement: The data presented in this study are openly available on GitHub at <https://github.com/tamasorosz/pyfemm>, accessed on 16 September 2025

Conflicts of Interest: The authors declare no conflicts of interest.

Abbreviations

The following abbreviations are used in this manuscript:

EOL	End of Life
CE	Circular Economy
EEA	European Environmental Agency
REE	Rare Earth Element
PM	Permanent Magnet
PMa-SynRM	Permanent Magnet-Assisted Synchronous Reluctance Machine
PMSM	Permanent Magnet Synchronous Machine
FI-PMa-SynRM	Flux-Intensifying Permanent Magnet-Assisted Synchronous Reluctance Machine
MFB	Magnet Flux Barrier
CFB	Cut-off Flux Barrier
IFB	Internal Flux Barrier
FEA	Finite Element Analysis

References

1. Goldman Sachs. Electric Vehicles are Forecast to be Half of Global Car Sales by 2035. 2023. Available online: <https://www.goldmansachs.com/insights/articles/electric-vehicles-are-forecast-to-be-half-of-global-car-sales-by-2035> (accessed on 16 September 2025).
2. Deloitte. Global Automotive Consumer Study. 2023. Available online: <https://www2.deloitte.com/us/en/pages/consumer-business/articles/global-automotive-consumer-study.html> (accessed on 16 September 2025).
3. European Environment Agency. *Electric Vehicles from Life Cycle and Circular Economy Perspectives—TERM 2018—Transport and Environment Reporting Mechanism (TERM) Report*; Publications Office: Luxembourg, 2018. [CrossRef]
4. Katona, M.; Orosz, T. Circular Economy Aspects of Permanent Magnet Synchronous Reluctance Machine Design for Electric Vehicle Applications: A Review. *Energies* **2024**, *17*, 1408. [CrossRef]
5. Schlesinger, L.; Koller, J.; Oechsle, O.; Molenda, P. Remanufacturing of E-mobility Components - Five-Step Implementation Strategy to increase Sustainability within Circular Economy. In Proceedings of the 2021 11th International Electric Drives Production Conference (EDPC), Online, 7–9 December 2021; pp. 1–8. [CrossRef]
6. Tiwari, D.; Miscandlon, J.; Tiwari, A.; Jewell, G.W. A Review of Circular Economy Research for Electric Motors and the Role of Industry 4.0 Technologies. *Sustainability* **2021**, *13*, 9668. [CrossRef]
7. Katona, M.; Orosz, T. Robustness of a flux-intensifying permanent magnet-assisted synchronous reluctance machine focusing on shifted surface-inset ferrite magnets. *Comput. Struct.* **2025**, *316*, 107845. [CrossRef]
8. Li, Z.; Hamidi, A.S.; Yan, Z.; Sattar, A.; Hazra, S.; Soulard, J.; Guest, C.; Ahmed, S.H.; Tailor, F. A circular economy approach for recycling Electric Motors in the end-of-life Vehicles: A literature review. *Resour. Conserv. Recycl.* **2024**, *205*, 107582. [CrossRef]
9. Jeong, C.; Park, J.; Bianchi, N. Alternatives to Replace Rare-Earth Permanent Magnet Motors in Direct Drive Applications. In Proceedings of the 2020 International Symposium on Power Electronics, Electrical Drives, Automation and Motion (SPEEDAM), Virtual, 24–26 June 2020; pp. 276–281. [CrossRef]
10. De Gennaro, M.; Jürgens, J.; Zanon, A.; Gragger, J.; Schlemmer, E.; Fricassè, A.; Marengo, L.; Ponick, B.; Olabarri, E.T.; Kinder, J.; et al. Designing, prototyping and testing of a ferrite permanent magnet assisted synchronous reluctance machine for hybrid and electric vehicles applications. *Sustain. Energy Technol. Assess.* **2019**, *31*, 86–101. [CrossRef]
11. Shao, L.; Tavernini, D.; Hartavi Karci, A.E.; Sorniotti, A. Design and optimisation of energy-efficient PM-assisted synchronous reluctance machines for electric vehicles. *IET Electr. Power Appl.* **2023**, *17*, 788–801. [CrossRef]
12. European Commission. Towards a Fast-Uptake of mEdium/Low-Voltage eLectric Power Trains (TELL). Grant Agreement ID: 824254. Available online: <https://cordis.europa.eu/project/id/824254> (accessed on 16 September 2025).
13. Ngo, D.K.; Hsieh, M.F.; Huynh, T.A. Torque Enhancement for a Novel Flux Intensifying PMa-SynRM Using Surface-Inset Permanent Magnet. *IEEE Trans. Magn.* **2019**, *55*, 1–8. [CrossRef]
14. Hsieh, M.F.; Ngo, D.K.; Thao, N.G.M. Flux Intensifying Feature of Permanent Magnet Assisted Synchronous Reluctance Motor with High Torque Density. *Electronics* **2022**, *11*, 397. [CrossRef]
15. Ngo, D.K.; Hsieh, M.F.; Dung Le, T. Analysis on Field Weakening of Flux Intensifying Synchronous Motor Considering PM Dimension and Armature Current. *IEEE Trans. Magn.* **2021**, *57*, 1–5. [CrossRef]

16. Hsieh, M.F.; Ngo, D.K.; Do, V.V.; Wu, C.H.; Wu, Y.K. Inductance Calculation of Flux Intensifying PMa-SynRM by Equivalent Magnetic Circuit. In Proceedings of the 2022 7th National Scientific Conference on Applying New Technology in Green Buildings (ATiGB), Da Nang, Vietnam, 11–12 November 2022; pp. 135–140. [CrossRef]
17. Liu, G.; Du, X.; Zhao, W.; Chen, Q. Reduction of Torque Ripple in Inset Permanent Magnet Synchronous Motor by Magnets Shifting. *IEEE Trans. Magn.* **2017**, *53*, 1–13. [CrossRef]
18. Du, X.; Liu, G.; Chen, Q.; Xu, G.; Xu, M.; Fan, X. Optimal Design of an Inset PM Motor With Assisted Barriers and Magnet Shifting for Improvement of Torque Characteristics. *IEEE Trans. Magn.* **2017**, *53*, 1–4. [CrossRef]
19. Luu, P.T.; Lee, J.Y.; Hwang, W.; Woo, B.C. Cogging Torque Reduction Technique by Considering Step-Skew Rotor in Permanent Magnet Synchronous Motor. In Proceedings of the 2018 21st International Conference on Electrical Machines and Systems (ICEMS), Jeju, Republic of Korea, 7–10 October 2018; pp. 219–223. [CrossRef]
20. Abbaszadeh, K.; Rezaee Alam, F.; Teshnehab, M. Slot opening optimization of surface mounted permanent magnet motor for cogging torque reduction. *Energy Convers. Manag.* **2012**, *55*, 108–115. [CrossRef]
21. Ling, J.M.; Nur, T. Influence of edge slotting of magnet pole with fixed slot opening width on the cogging torque in inset permanent magnet synchronous machine. *Adv. Mech. Eng.* **2016**, *8*, 1687814016659598. [CrossRef]
22. Nur, T.; Mulyadi, M. Improve cogging torque method in inset-permanent magnet synchronous machine. In Proceedings of the 2018 IEEE International Conference on Applied System Invention (ICASI), Chiba, Japan, 13–17 April 2018; pp. 1211–1213. [CrossRef]
23. Nur, T.; Herlina. Enhancement of Cogging Torque Reduction on Inset Permanent Magnet Generator by Using Magnet Edge Shaping Method. In Proceedings of the 2018 International Conference on Electrical Engineering and Computer Science (ICECOS), Pangkal Pinang, Indonesia, 2–4 October 2018; pp. 429–434. [CrossRef]
24. Orosz, T. p2femm. 2024. Available online: <https://github.com/tamasorosz/py2femm> (accessed on 16 September 2025).
25. Meeker, D. FEMM 4.2—Finite Element Method Magnetics. 2020. Available online: <https://www.femm.info/wiki/HomePage> (accessed on 16 September 2025).
26. Katona, M.; Bánya, D.G.; Németh, Z.; Kuczmann, M.; Orosz, T. Remanufacturing a Synchronous Reluctance Machine with Aluminum Winding: An Open Benchmark Problem for FEM Analysis. *Electronics* **2024**, *13*, 727. [CrossRef]
27. Zhang, Q.; Couloigner, I. A New and Efficient K-Medoid Algorithm for Spatial Clustering. In Proceedings of the Computational Science and Its Applications—ICCSA 2005, Singapore, 9–12 May 2005; Gervasi, O., Gavrilova, M.L., Kumar, V., Laganà, A., Lee, H.P., Mun, Y., Taniar, D., Tan, C.J.K., Eds.; Springer: Berlin/Heidelberg, Germany, 2005; pp. 181–189.
28. Bushra, A.A.; Yi, G. Comparative Analysis Review of Pioneering DBSCAN and Successive Density-Based Clustering Algorithms. *IEEE Access* **2021**, *9*, 87918–87935. [CrossRef]
29. Barri, D.; Soresini, F.; Gobbi, M.; Gerlando, A.d.; Mastinu, G. Optimal design of Traction Electric Motors by a new Adaptive Pareto Algorithm. *IEEE Trans. Veh. Technol.* **2025**, *74*, 8890–8906. [CrossRef]
30. Liu, Q.; Ma, J.; Zhao, X.; Zhang, K.; Xiangli, K.; Meng, D. A novel method for fault diagnosis and type identification of cell voltage inconsistency in electric vehicles using weighted Euclidean distance evaluation and statistical analysis. *Energy* **2024**, *293*, 130575. [CrossRef]
31. Nazari, M.; Hussain, A.; Musilek, P. Applications of Clustering Methods for Different Aspects of Electric Vehicles. *Electronics* **2023**, *12*, 790. [CrossRef]
32. Zheng, L.; Jia, K.; Wu, W.; Liu, Q.; Bi, T.; Yang, Q. Cosine Similarity Based Line Protection for Large Scale Wind Farms Part II—The Industrial Application. *IEEE Trans. Ind. Electron.* **2022**, *69*, 2599–2609. [CrossRef]
33. Miah, M.S.U.; Sulaiman, J.; Sarwar, T.B.; Zamli, K.Z.; Jose, R. Study of Keyword Extraction Techniques for Electric Double-Layer Capacitor Domain Using Text Similarity Indexes: An Experimental Analysis. *Complexity* **2021**, *2021*, 8192320. [CrossRef]
34. Zhang, C.; Zhao, S.; Yang, Z.; He, Y. A multi-fault diagnosis method for lithium-ion battery pack using curvilinear Manhattan distance evaluation and voltage difference analysis. *J. Energy Storage* **2023**, *67*, 107575. [CrossRef]
35. Bayindir, R.; Yesilbudak, M.; Colak, I.; Sagiroglu, S. Excitation Current Forecasting for Reactive Power Compensation in Synchronous Motors: A Data Mining Approach. In Proceedings of the 2012 11th International Conference on Machine Learning and Applications, Boca Raton, FL, USA, 12–15 December 2012; Volume 2, pp. 521–525. [CrossRef]
36. Lim, Y.F.; Teoh, S.S. Automatic Detection of Hotspots on Electric Motors Using Thermal Imaging. In Proceedings of the 11th International Conference on Robotics, Vision, Signal Processing and Power Applications, Penang, Malaysia, 5–6 April 2021; Mahyuddin, N.M., Mat Noor, N.R., Mat Sakim, H.A., Eds.; Springer: Singapore, 2022; pp. 1035–1040.
37. Rai, R.; Grover, J. Comparative Analysis of Cosine and Jaccard Similarity-Based Classification for Detecting CAN Bus Attacks. In Proceedings of the 2024 IEEE Region 10 Symposium (TENSYMP), New Delhi, India, 27–29 September 2024; pp. 1–6. [CrossRef]
38. GLOWACZ, A. Diagnostics of Synchronous Motor Based on Analysis of Acoustic Signals with the use of Line Spectral Frequencies and K-nearest Neighbor Classifier. *Arch. Acoust.* **2014**, *39*, 189–194. [CrossRef]
39. Pietrzak, P.; Wolkiewicz, M. Demagnetization Fault Diagnosis of Permanent Magnet Synchronous Motors Based on Stator Current Signal Processing and Machine Learning Algorithms. *Sensors* **2023**, *23*, 1757. [CrossRef] [PubMed]

40. Junior, R.F.R.; de Almeida, F.A.; Jorge, A.B.; Pereira, J.L.J.; Francisco, M.B.; Gomes, G.F. On the use of the Gaussian mixture model and the Mahalanobis distance for fault diagnosis in dynamic components of electric motors. *J. Braz. Soc. Mech. Sci. Eng.* **2023**, *45*, 139. [[CrossRef](#)]
41. Puggini, L.; Doyle, J.; McLoone, S. Fault Detection using Random Forest Similarity Distance. *IFAC-PapersOnLine* **2015**, *48*, 583–588. [[CrossRef](#)]

Disclaimer/Publisher’s Note: The statements, opinions and data contained in all publications are solely those of the individual author(s) and contributor(s) and not of MDPI and/or the editor(s). MDPI and/or the editor(s) disclaim responsibility for any injury to people or property resulting from any ideas, methods, instructions or products referred to in the content.